Energy 134 (2017) 35–49

Contents lists available at ScienceDirect

Energy

journal homepage: www.elsevier.com/locate/energy

Experimental and modeling investigation of an organic Rankine cycle system based on the scroll expander

Zheng Miao, Jinliang Xu*, Kai Zhang

The Beijing Key Laboratory of Multiphase Flow and Heat Transfer for Low Grade Energy Utilization, North China Electric Power University, Beijing, 102206, PR China

ARTICLE INFO

Article history:
Received 20 January 2017
Received in revised form
11 May 2017
Accepted 1 June 2017
Available online 1 June 2017

Keywords:
Organic Rankine cycle
Scroll expander
Experimental
Modeling
Optimization

ABSTRACT

A comprehensive model for organic Rankine cycle (ORC) was presented in this work. Several sub-models were included. Fewer empirical coefficients were needed in the improved expander model than the previous one as several parameters were obtained directly from the actual structure parameters of scrolls. The Dalton's law was used to simulate the pressure in the liquid tank, consisting of partial pressures of non-condensable gas and saturated vapor. A spray cooling tower model was built to take account of the influence of environment temperature and humidity on the ORC operation and performance. The simulations agree well with the tested data. Then, the model was used to analyze the mismatch among components of the cycle and evaluated the potential optimizations to the ORC prototype. For the present ORC system, the model predicts that the output power can be doubled after the optimization measures are taken. The environment temperature and humidity apparently influence the system performance. The effect of humidity becomes significant at high environment temperature. The expander power can be decreased by one third when the humidity is increased from 50% to 90% in summer season. The present work provides the guidance for design and operation of the ORC system.

1. Introduction

Energy shortage and environment protection are leading to rapidly growing interest in the utilization of low grade energy, especially for the heat sources with temperature below 250 °C. The steam based Rankine cycle is not applicable for low grade energy conversion due to its high boiling temperature. However, organic Rankine cycle (ORC) is regarded as the promising technology to convert low grade heat into work [1–3].

During the past two decades, ORC has been widely investigated experimentally and theoretically. Regarding the experimental studies, Yamanoto et al. [4] experimentally studied an ORC system based on a micro-turbine with R123 as the working fluid. Li et al. [5] analyzed the effect of mass flow rate of the working fluid on the thermal efficiency of a regenerative ORC. The achieved thermal efficiency was 7.98% at the heat source temperature of 130 °C. In Refs. [6–8], a kW-scale ORC with a specially designed turbine was tested, and the maximum expander isentropic efficiency of 65% and the cycle thermal efficiency of 6.8% were obtained. Bracco et al. [9] developed a domestic-scale ORC with R245fa as the working fluid. The electric efficiency was about 8% at the expander inlet temperature ranging from 120 to 150 °C. Minea [10] tested a 50kWe ORC prototype using a twin screw expander. The electric efficiency was 6.62–7.57% at the heat source temperature from 85 to 116 °C. Wang et al. [11–13] experimentally studied a solar recuperative ORC system using R245fa and zeotropic mixtures. They tested the performance of a kW-scale rolling-piston expander. The thermal efficiency was 5–6%. Li et al. [14] tested a kW-scale ORC system with a turbo-expander and claimed that both the heat source temperature and pump speed were important parameters in determining system thermal efficiency and the component operations. Uusitalo et al. [15] conducted an experimental investigation of a ORC system driven by heat from the diesel engine exhaust. No power was extracted from the system as an expansion valve is used instead of a real expander. The effective removal of non-condensable gases during the operation was pointed out to be a challenge in achieving the targeted power output. In our previous work, we developed an ORC prototype based on a 4 kW scroll expander [16–18]. Both steady and dynamic operation characteristics were provided at the heat source temperature from 140 to 160 °C. It is found that the obtained shaft powers significantly deviated from calculated ones,

* Corresponding author.
E-mail address: xjl@ncepu.edu.cn (J. Xu).

http://dx.doi.org/10.1016/j.energy.2017.06.001
0360-5442/

which are calculated based on the enthalpies under measured vapor temperatures and pressures at the expander inlet and outlet. In summary, the available experimental investigations of ORCs focused on small scale power output. Few developed ORCs were optimized due to the lack of knowledge on the mismatch among components of the cycle and the difficulty in modifying the tested prototype.

Reliable mathematical model is a powerful and economical tool to investigate the ORC system, and it can be used to study the mismatch among components and evaluate potential optimizations to the system. In nowadays, most theoretical analysis of the ORC is based on the thermodynamic analysis which is quite different from the modeling. In the thermodynamic analysis, the first and second laws of thermodynamics are used to analyze the operation parameters and performance of ORCs [1,19–28]. Such analysis is carried out at the system level, aiming at the "design" of a new system, and does not consider the influence of heat transfer or heat-power conversion process in the practical equipments. Thus, the analysis is relatively idealized. Alternatively, in the mathematical models, both the system level and the detailed processes of heat transfer and heat-power conversion are included, focusing on the "operation" analysis and optimization under the constraints of practical equipments. So far, the mathematical models have seldom been reported in the literature for ORCs. Wei et al. [29] proposed a dynamic mathematical model of an ORC system, using the moving boundary model for heat exchangers and empirical model for pump and expander. Lemort et al. [30–32] integrated an open-drive oil-free scroll expander into an ORC system. The simulation results revealed that the heat loss, internal leakage and mechanical induced exergy destructions mainly accounted for the deteriorated expander performance. Benoto et al. [33] performed an analysis of hot spots in boilers of ORC units during transient operation. The heat exchanger model used a distributed cross-flow physical topology and local correlations for single- and two-phase heat transfer coefficients. Proctor et al. [34] proposed a dynamic modeling of a commercial scale geothermal ORC power plant using the process simulation software VMGSim. The model was expected to test potential improvements to the system. Dong et al. [35] presented a semi-empirical model to optimize the experimental system and obtain an optimum design method of ORC system. Two experimental systems were built up; one was for providing data to the semi-empirical model and the other was for model validation. Recently, Ziviani et al. [36] performed a test of an ORC system with a single-screw expander and a control-oriented steady-state model of the system to optimized the operation of the ORC unit. The frequency of the pump is used as controlled variable to adjust the superheating level for different working conditions. It is noted that these models should be further improved to reflect the practical operation of the ORC system. For example, the non-condensable gas was observed in test [17,30], but it was not included in the modeling. Furthermore, the influence of the environment conditions on ORC operation and performance is rarely studied [37].

The objective of this paper is to provide a comprehensive numerical model based on practical situations. Several sub-models were included. New models were proposed for the liquid tank and the spray cooling tower to evaluate the influences of non-condensable gas and environment conditions. The heat transfer model of evaporator and condenser is a three-zone model (subcooled liquid, two-phase and superheated vapor). Different heat transfer correlations are used for different zones. An expander model was developed based on the model of Lemort et al. [30] but using fewer empirical parameters. The numerical results matched the measured data of the ORC system. For the present built ORC system, the predicted shaft power by this model can be doubled after the system optimization. The environment temperature and humidity apparently influence the system performance.

2. The tested ORC system

2.1. System description

Fig. 1 shows the design chart of the ORC system, the *T-s* diagram of the cycle at the design point and photos of the prototype in this study. It consists of five subunits: the conductive oil circuit (red lines), the working fluid R123 circuit (brown lines), the cooling water circuit (blue lines), the lubricant oil circuit (green lines) and the AC dynamometer unit. The detailed information about this system can be found in our former work [17]. The *T-s* diagram in Fig. 1(b) represent the design point of the ORC prototype. The points 1 and 2 refer to the start and end of the expansion process, respectively. The isentropic efficiency of the expander was expected to be 0.7. Thus, the expander power is 3.85 kW under the enthalpy difference between points 1 and 2, and the corresponding mass flow rate of the organic fluid is 680 kg/h. The efficiency of the pump was expected to be 0.5. In this condition, the evaporator load is about 37.3 kW.

The conductive oil is used to simulate the low grade heat source. The heat flux absorbed by R123 in the evaporator is given as:

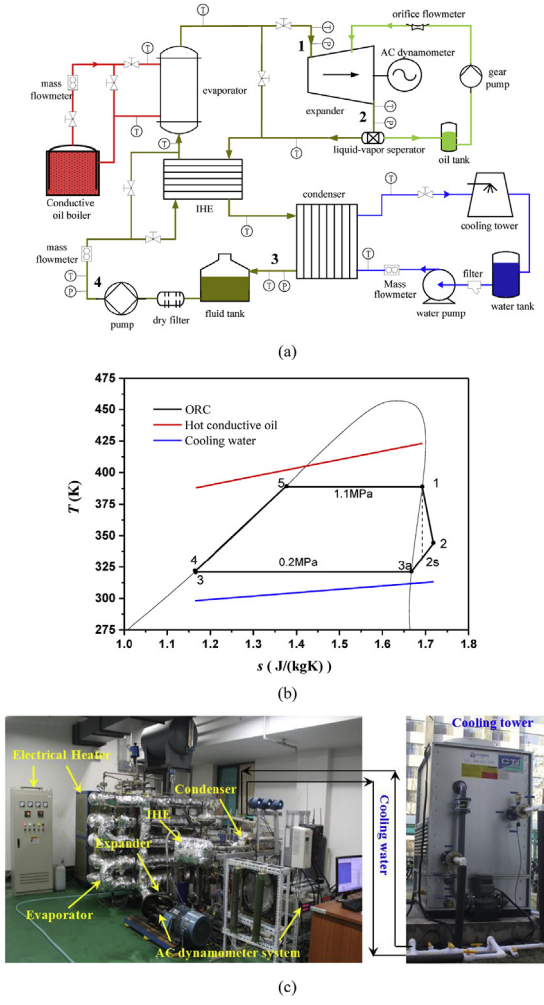

Fig. 1. (a) Design of the ORC system, (b) *T-s* diagram of the cycle, and (c) photos of the experimental setup.

$$Q = m(H_{eva,out} - H_{eva,in}) \quad (1)$$

The expander in this prototype is modified from a scroll compressor originally used in the bus air conditioning system by removing the one-way valve at the discharge port of the fixed scroll. An AC dynamometer unit is adopted to measure and control the rotating speed and shaft torque of the expander. Thus, the output power of the expander is

$$W_{t,me} = N_t \times T_t / 9.55 \quad (2)$$

The working fluid is circulated by a piston pump. The power consumed by the pump can be obtained from the frequency converter which controls the pump. In such a way, the measured output power and thermal efficiency are

$$W_{me} = W_{t,me} - W_{p,me} \quad (3)$$

$$\eta_{me} = \frac{W_{t,me} - W_{p,me}}{Q} \quad (4)$$

The location of sensors in the present ORC system can be found in Fig. 1(b). The detailed information of the tested ORC system, sensors and error analysis can be found in our former work [17].

2.2. Testing procedure

The operation of the ORC system is specified by two accessible and independent parameters: the R123 mass flow rate and the external load of the expander (the shaft torque or the rotating speed). These two parameters were adjusted through two frequency converters, one for the fluid pump and the other for the expander. Performance at the conductive oil temperatures of 150 °Cwas tested. Table 1 shows the main operation parameters. At each R123 mass flow rate, the shaft torque of the expander is changed while the mass flow rate and temperature of conductive oil as well as the mass flow rate of cooling water are kept constant.

3. Mathematical model

In this section, models of components in the ORC loop, corresponding to the tested prototype in section 2, are introduced. Assumptions adopted in the mathematical model are given as followed:

(1) During the phase change in the heat exchanger, the liquid and vapor phases are at the thermodynamic equilibrium state.
(2) In the two-phase zone of the heat exchangers, the liquid and vapor phases have the same velocity.
(3) The non-condensable gas and vapor of working fluid in the tank are both treated as the ideal gas. And the amount of non-condensable gas in the tank is constant.

Table 1
Major operating parameters in the test.

Operating parameters	Value
Air temperature	0–10 °C
Temperature of the conductive oil	150 °C
Mass flow rate of the conductive oil	2005–2035 kg/h
Temperature of the cooling water	13.7–25.7 °C
Mass flow rate of the cooling water	2580–2610 kg/h
shaft torque	10%–70% of the maximum value
R123 pumping frequency	7.0–11.0 Hz

(4) The pressure drops in evaporator and condenser are relatively small, and are treated as constant values of 20 kPa and 10 kPa, respectively. The pressure drop in pipes between different components is neglected.

3.1. Model of the tank

A 0.08 m^3 tank is installed between the condenser and the R123 pump as a buffer unit. It is found in the test that the pressure in the tank is significantly higher than the saturated pressure corresponding to the liquid temperature. Thus, the effect of non-condensable gas in the loop should be considered. It is assumed that the amount of non-condensable gas in the tank is constant. So the pressure in the tank can be calculated by the classical Dalton's law:

$$P_{tank} = P_{sat} + n_{gas}RT \Big/ \left(V_{tank} - V_{liquid}\right) \quad (5)$$

where n_{gas} is obtained from the tested data. During the calculation, the variation of V_{liquid} is derived from the model of exchangers by calculating the liquid volume in the evaporator and condenser.

3.2. Model of the closed spray cooling tower

The closed spray cooling tower is used to release heat to the environment. There are ten rows of tubes in the tower, and each row has eighteen tubes. The cooling water flows in the tube. The deluge water is sprayed from the top to the tube bundle while the air flows on the opposite direction. Considering the computational time, each row of tubes is treated as a block. Thus, the heat release process in the cooling tower can be calculated by a one-dimensional model considering the heat transfer from the cooling water in the tube to the deluge water out the tube, from the deluge water to the air, and during the evaporation of the deluge water. The heat transfer from the cooling water to the deluge water in a certain row can be expressed as:

$$Q_{cw} = m_{cw}c_{p,cw}\left(T_{cw,in} - T_{cw,out}\right)_i = AK_i(T_{cw} - T_{dw})_i \quad i = 1\ldots10 \quad (6)$$

The heat transfer from the deluge water to the air in each row can be written as [38]:

$$Q_{air} = hA(T_{dw} - T_{air})_i + i_v h_d A(\omega_s - \omega)_i \quad (7)$$

where the first term on the right of Eq. (7) represents the convective heat transfer from the deluge water to the air and is given as:

$$hA(T_{dw} - T_{air})_i = m_{air}c_{p,air}\left(T_{air,out} - T_{air,in}\right)_i \quad (8)$$

The second term on the right of Eq. (7) denotes heat transfer during the evaporation of the deluge water. The mass flux due to the evaporation of the deluge water is calculated by:

$$h_d A(\omega_s - \omega)_i = m_{air}(\omega_{out} - \omega_{in})_i \quad (9)$$

Parameters and other correlations used in the above equations are given in Table 2 [38–40].

3.3. Model of the scroll expander

The scroll expander model is developed based on a semi-empirical model proposed by Lemort et al. [30]. Several parameters used in this model should be identified by the experimental data. We modified the model based on the practical structure of the

Table 2
Parameters used in the model of cooling tower.

Parameters	Unit	Expressions
Overall heat transfer coefficient	W/(m^{2}K)	$\frac{1}{K}=\frac{1}{h_i}\frac{d_o}{d_i}+r_i\frac{d_o}{d_i}+\frac{d_o}{2\lambda}\ln\left(\frac{d_o}{d_i}\right)+r_o+\frac{1}{h_o}$
In-tube convective heat transfer coefficient	W/(m^{2}K)	$h_i=0.023\frac{\lambda_p}{d_i}\mathrm{Re}^{0.8}\mathrm{Pr}^{0.3}$
Out-tube convective heat transfer coefficient	W/(m^{2}K)	$h_o=704(1.39+0.022T_w)\left(\frac{m_w}{d_o}\right)^{1/3}$
Mass transfer coefficient	kg/m^2	$h_d=0.049G_{ma}^{0.905}$
Lewis factor		$Le=h/(c_{p,air}h_d)=1$
Saturated pressure corresponding to the dry-bulb temperature	Pa	$P_V=611.2e^{\frac{\left(18.678-\frac{T}{234.5}\right)T}{T+257.14}}$
Moisture content	%	$\omega=0.6219\frac{0.01H_rP_v}{101326-0.01H_rP_v}$
Enthalpy of the moist air	kJ/kg	$H_{air}=1.01T_d+(2500+1.84T_d)\omega$

expander used in our test, mainly in 3 aspects. Firstly, as the scroll expander is refitted from a compressor, the evolution of refrigerant through the expansion process is modified according to the expander structure and shown in Fig. 2(a):

step1: supply cooling-down (su-su1), representing the heat loss of R123 vapor from the supply pipe line to suction port on the scroll;
step2: supply pressure drop (su1-su2), representing the pressure drop of R123 vapor flowing through the suction port on the scroll;
step3: isentropic expansion according to the built-in volume ratio (s);
step4: adiabatic expansion under the exhaust pressure (v), considering the discharge of R123 at the end of expansion and the process of under-/over-expansion;
step5: mixing of the leakage flow to the mainstream (ex2-ex1);
step6: exhaust heat transfer (ex1-ex), representing the heating or cooling of R123 vapor from the discharge chamber to pipe line.

Secondly, the heat transfer shown in Fig. 2(a) is treated as a process having definite physical meaning, and includes two aspects: one is the heat transfer between the expander shell and the ambient, the other is that inside the expander. The temperature distribution of expander is divided into two zones based on the

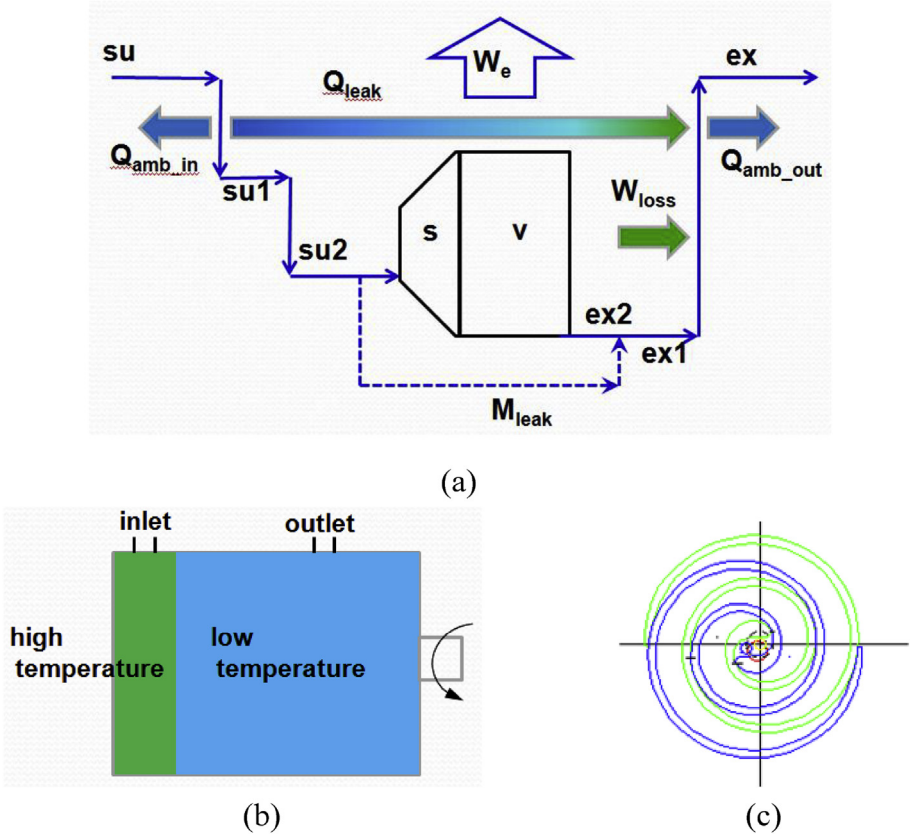

Fig. 2. (a) Scheme of the expander model, (b) temperature zones of the expander and (c) representation of the scrolls.

fluid temperature, which can be seen in Fig. 2(b). The bottom of the fixed scroll is the dividing line between the two zones. The high temperature zone is near to the inlet. The heat loss from the shell to the ambient can be treated as the natural convection or mixed convection heat transfer.

$$Q_{amb,h} = A_h h_{amb}(T_{su} - T_{amb}) \tag{10}$$

$$Q_{amb,l} = A_l h_{amb}(T_{ex1} - T_{amb}) \tag{11}$$

The heat transfer inside the expander from the high temperature zone to the low temperature zone is related to the heat transfer between the scrolls and fluid. It can be described as:

$$Q_{leak} = Ah_{in}(T_{su} - T_{ex1}) \tag{12}$$

$$Ah_{in} = \xi m^{0.8} \tag{13}$$

Thirdly, we obtain the built-in volume ratio r_{exp} and the swept volume V_s based on the geometry of the scrolls, shown in Fig. 2(c). Through the three modifications above, the number of empirical parameters which need to be identified by the tested data can be reduced from 9 to 5. Parameters used in the expander model are given in Table 3.

Corresponding to evolution steps of the refrigerant during the expansion, the expander model is described as follows.

At step 1: supply cooling-down (su-su1) and step 6 exhaust heat transfer (ex1-ex), we get

$$H_{su1} = H_{su} - Q_{amb,h} - Q_{leak} \tag{14}$$

$$H_{ex} = H_{ex1} + Q_{leak} + W_{loss} - Q_{amb,l} \tag{15}$$

where W_{loss} is the loss of shaft power caused by friction in the expander and can be calculated by:

$$W_{loss} = 2\pi \cdot N \cdot T_{loss} \tag{16}$$

At step 2: supply pressure drop (su1-su2), the process of fluid flowing through the suction port is treated as the isentropic flow through a converging nozzle. It is described as:

$$H_{su2} = H_{su1} - \left(\frac{mv}{A_{su}}\right)^2 \Big/ 2 \tag{17}$$

The same treatment is applied to the calculation of the leakage mass flow rate:

Table 3
Parameters used in the model of scroll expander.

Parameters	
Geometry parameters	
Scroll turns	2.5
Height of the scroll profile	50 mm
Thickness of the scroll profile	4.8 mm
Pitch of the scroll profile	26.5 mm
Radius of the expander	170 mm
Length of the expander	281 mm
Built-in volume ratio r_{exp}	2.27
Swept volume V_s	1.19×10^{-4}m^3
Empirical parameters identified by tested data	
Supply port area A_{su}	6.1×10^{-5}m^2
Leakage area A_{leak}	7.0×10^{-6}m^2
Heat transfer coefficient with the ambient h_{amb}	19W/(m^{2}K)
Coefficient ξ related with Ah_{in}	0.24
Mechanical loss torque T_{loss}	5.5N·m

$$m_{leak} = \frac{A_{leak}}{v_{leak}}\sqrt{2(H_{su2} - H_{leak})} \tag{18}$$

The internal mass flow rate is calculated based on the swept volume of the expander:

$$m_{in} = \frac{NV_s}{v_{su2}} \tag{19}$$

And $m = m_{in} + m_{leak}$ is the convergence criterion of the expander model.

At step 3: isentropic expansion according to the built-in volume ratio and step 4: adiabatic expansion under the exhaust pressure, same to the assumption in Lemort's work [30] on treating under- or over-expansion, the energy balance is given as follows,

$$m_{ex2}u_{ex2} - m_{in}u_{ad} = (m_{ex2} - m_{in})H_{ex2} \tag{20}$$

V_{ad} is expressed as

$$V_{ad}N = m_{in}v_{ad} = m_{ex2}v_{ex2} \tag{21}$$

Substituting Eq. (21) into Eq. (20), the specific enthalpy H_{ex2} is derived as:

$$H_{ex2} = H_{ad} - v_{ad}(p_{ad} - p_{ex2}) \tag{22}$$

Accordingly, the expander shaft power and isentropic efficiency can be got as:

$$W_{exp} = m_{in}(H_{su2} - H_{ex2}) - W_{loss} \tag{23}$$

$$\eta_{exp} = \frac{W_{exp}}{m(H_{su} - H_{ex,s})} \tag{24}$$

At step 5: mixing of the leakage flow to the mainstream, the energy balance is given as:

$$mH_{ex1} = m_{in}H_{ex2} + m_{leak}H_{leak} \tag{25}$$

Herein, the temperature T_{ex1} is determined by the specific enthalpy H_{ex1} and the pressure p_{ex2}.

3.4. Models of the heat exchangers

Two heat exchangers are simulated in the present model. The evaporator is a double-pipe heat exchanger and the condenser is a plate heat exchanger. In the heat exchanger model, the heat transfer process is divided into three zones: the liquid zone, the two-phase zone and the vapor zone. Then, each zone is further subdivided into small sections, shown in Fig. 3. The arrangement of those two heat exchangers is counter flow. And the heat transfer in each zone is calculated by a one-dimensional model.

3.4.1. Evaporator

For the heat transfer in single phase zone in the evaporator, including the preheating zone and the superheating zone, the same correlation of convective heat transfer coefficient is adopted for both the working fluid side and the oil side. In the form of Nusselt number Nu, it is given as the classical Gnielinski correlation [41]:

$$Nu = \frac{(f/8)(\mathrm{Re} - 1000)\mathrm{Pr}}{1 + 12.7\sqrt{f/8}(\mathrm{Pr}^{2/3} - 1)}\left[1 + \left(\frac{d}{l}\right)^{2/3}\right]c_t \tag{26}$$

$$f = (1.82\lg\mathrm{Re} - 1.64)^{-2} \tag{27}$$

For the heat transfer in two-phase zone, the convective heat

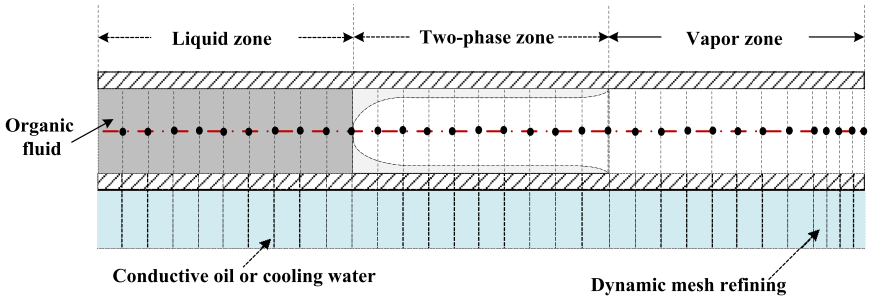

Fig. 3. Scheme of zones and meshing of the heat exchanger model.

transfer coefficient is calculated from correlations proposed by Gungor and Winterton [42–44]:

$$h_{tp} = Eh_L + Sh_{nb} \tag{28}$$

$$h_L = 0.023\mathrm{Re}_L^{0.8}\mathrm{Pr}_L^{0.4}\left(\frac{k_L}{d_i}\right) \tag{29}$$

$$h_{nb} = 55p_r^{0.12}(-0.4343\ln p_r)^{-0.55}M^{-0.5}q^{0.67} \tag{30}$$

Parameters used in Gungor and Winterton's model are given in Table 4.

3.4.2. Condenser

At the cooling water side, the convective heat transfer coefficient in the form of Nusselt number *Nu* is given as [45]:

$$Nu_w = 0.2121\mathrm{Re}_w^{0.78}\mathrm{Pr}_w^{1/3} \tag{31}$$

At the R123 side, the convective heat transfer coefficients in the liquid zone [46] and vapor zone are calculated by Eq. (32) and Eq. (33), respectively.

$$Nu = 0.317\mathrm{Re}^{0.703}\mathrm{Pr}^{1/3} \tag{32}$$

$$Nu = 0.2267\mathrm{Re}^{0.631}\mathrm{Pr}^{1/3} \tag{33}$$

The condensation heat transfer coefficient is estimated by the correlations below [45]:

$$Nu = 4.118\mathrm{Re}_{eq}^{0.4}\mathrm{Pr}^{1/3} \tag{34}$$

Table 4
Parameters used in Gungor and Winterton's model.

Parameters	Expression
Boiling number	$\mathrm{Bo} = \frac{q}{mh_{LG}}$
Martinelli parameter	$X_{tt} = \left(\frac{1-x}{x}\right)^{0.9}\left(\frac{\rho_G}{\rho_L}\right)^{0.5}\left(\frac{\mu_L}{\mu_G}\right)^{0.1}$
Liquid Reynolds number	$\mathrm{Re}_L = \frac{m(1-x)d_i}{\mu_L}$
Liquid Prandtl number	$\mathrm{Pr}_L = \frac{c_{pL}\mu_L}{k_L}$
The liquid Froude number	$\mathrm{Fr}_L = \frac{m}{\rho_L^2 g d_i}$
The two-phase convection multiplier	$E = 1 + 24000\mathrm{Bo}^{1.16} + 1.37\left(\frac{1}{X_{tt}}\right)^{0.86}$
The boiling suppression factor	$S = [1 + 0.00000115E^2\mathrm{Re}_L^{1.17}]^{-1}$
Multiplier to *E*	$E_2 = \mathrm{Fr}_L^{(0.1-2\mathrm{Fr}_L)}$
Multiplier to *S*	$S_2 = \mathrm{Fr}_L^{0.5}$

$$\mathrm{Re}_{eq} = \frac{G_{eq}d_h}{\mu_l} \tag{35}$$

$$G_{eq} = G\left[1 - X_m + X_m\left(\frac{\rho_l}{\rho_v}\right)^{1/2}\right] \tag{36}$$

where the equivalent mass flux G_{eq} was proposed by Akers et al. [47], and is a function of the fluid mass flux, mean quality and densities at the saturated condition.

3.5. Model of the R123 pump

The working fluid is circulated by a piston pump, which is controlled by a frequency converter. The frequency of 50 Hz corresponds to the volume flow rate of 2000 *l/h*. The mass flow rate of R123 in the present prototype is below 1000 kg/h. Thus, the pump works far from its design point. The pump efficiency varies with the mass flow rate and pressure difference. Consequently, an expression of the pump efficiency is proposed here, which sets the efficiency at the design flow rate of the pump as a reference value:

$$\eta_{Pump} = \eta_d\left(\frac{m}{m_d}\right)^n \tag{37}$$

Herein, $\eta_d = 0.84$ and $n = 0.341$ are identified by the tested data. It is noted that η_d is not the "design efficiency" of the pump but reference value identified by the tested data. Thus, the error of Eq. (37) will be larger if it is used at a R123 mass flow rate higher than 1000 kg/h. The consumed power by the pump can be calculated by

$$W_{pump} = W_H \big/ \eta_{Pump} \tag{38}$$

where W_H is the enthalpy-determined power consumed by the pump.

3.6. Model of the global cycle

By interconnecting the models of different components above, we get the global model of the cycle corresponding to the prototype introduced in section 2. Fig. 4 shows the block diagram of the global model. The program is developed in the Matlab environment, and the properties of the working fluid are obtained from REFPROP database software. Two parameters (in green) are the control variables of the model, the R123 mass flow rate and the expander rotating speed. Parameters in red are the performance of the system, shaft power of the expander, power consumed by the pump and heat fluxes in the evaporator and condenser. So the thermal efficiency of the cycle can be derived from

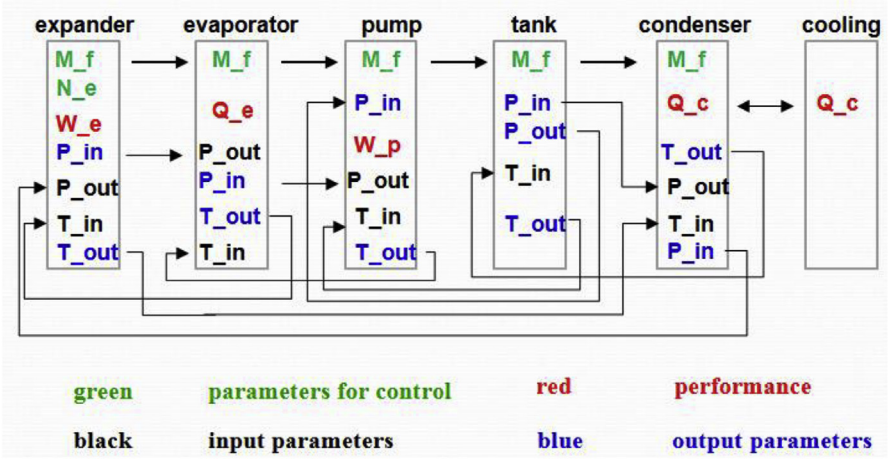

Fig. 4. Block diagram of the global ORC model.

$\eta = (W_{exp} - W_{pump})/Q_{evp}$. Parameters in black and blue are the variables transferred between different sub-models. The calculation of the model can start from any sub-model. In the present work, we start from the tank model by assuming the temperature at the tank inlet. The characteristics of heat carrier and cooling source are not shown in Fig. 3, and their information is given to the evaporator model and the condenser model.

A plate heat exchanger is installed in the prototype as a regenerator. However, in the present work, it only functions as the vapor phase flow channel because it is bypassed for the liquid phase, shown in Fig. 1. In this condition, the resistance to vapor flow from the expander outlet to the condenser inlet is considered in term of the pressure drop:

$$\Delta P = 2.55G^{1.7} \Big/ (2\rho_m) \tag{39}$$

$$G = \frac{m}{NA_c} \tag{40}$$

The pressure drops in evaporator and condenser are relatively small, and are treated as constant values of 20 kPa and 10 kPa, respectively. The pressure drop in pipes is neglected.

4. Results and discussion

4.1. Tested cycle performance

The operation characteristics and performance of the prototype in section 2 are tested at the oil temperature of 150 °C. Fig. 5 shows the trends of shaft power and thermal efficiency varying with expander rotating speed. The largest shaft power of 2645 W is obtained at the R123 mass flow rate of 550 kg/h. At the lower mass flow rate, 505 kg/h, the vapor cannot offer enough shaft torque for the expander, so the shaft power is also lower. The higher mass flow rate of R123 leads to the rapid decrease in the degree of superheat at the expander inlet. As mentioned in our former work, the liquid entrainment will occur at a relatively low degree of superheat. And the shaft power is also reduced. Compared to the design point in Fig. 1(b), it is seen that the real operation performance deviates from the designed thermodynamic performance. The irreversible losses caused by the friction in the expander, over- or under-expansion of the expander, heat loss from the expander wall to the environment, and pressure drop from the pipe to the expander chamber account for such deviation. On the one hand, the results in Fig. 5(a) indicate that the area of the evaporator should be increased for the operation of the prototype at a larger R123 mass flow rate. On the other hand, the match between the built-in volume ratio and the external pressure ratio should be analyzed and optimized. The trends of shaft power in Fig. 5(a) result in the gradual decrease

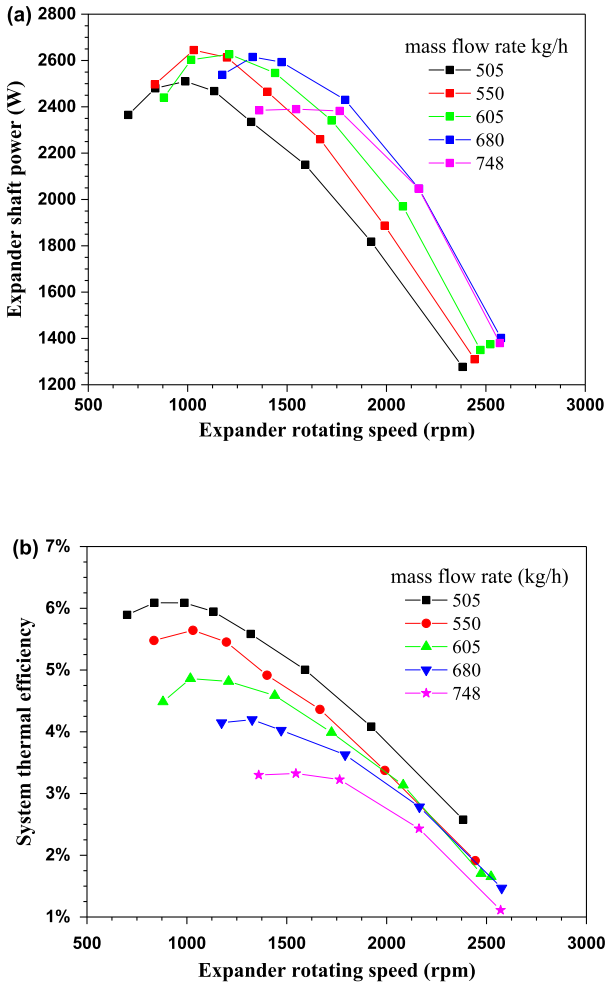

Fig. 5. Variation of the (a) shaft power and (b) thermal efficiency of the expander with different rotating speed.

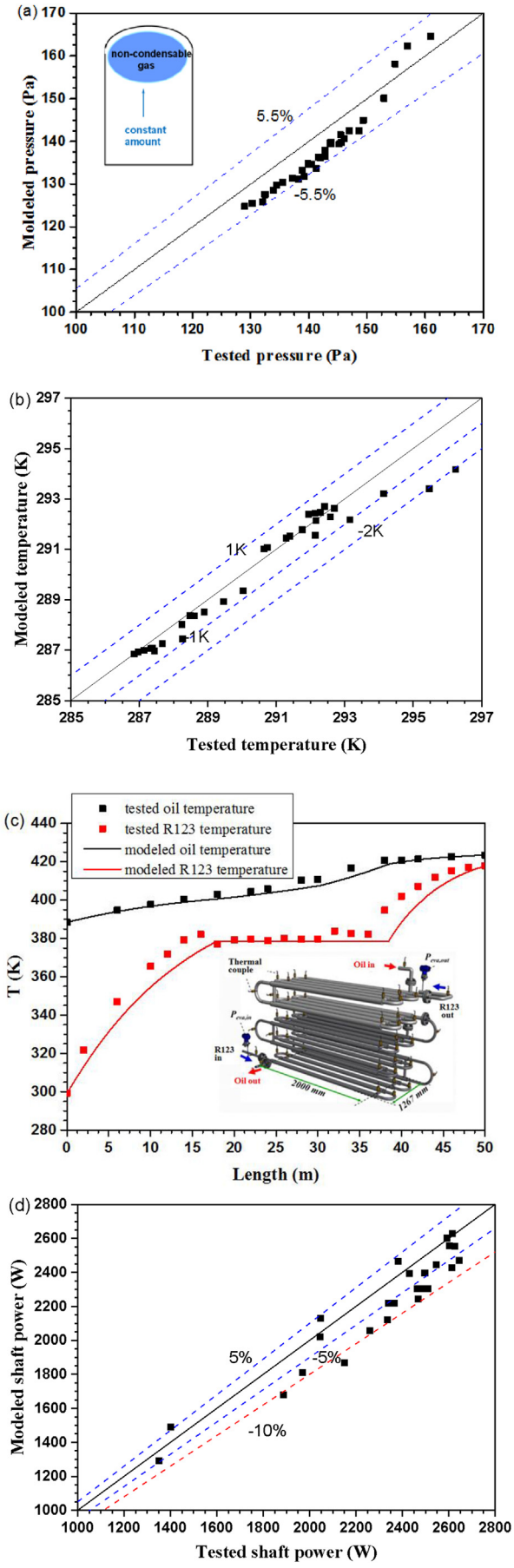

Fig. 6. Validations of (a) the tank model, (b) the cooling tower model, (c) the evaporator model and (d) the global ORC model.

in the thermal efficiency in Fig. 5(b) as the heat flux in the evaporator and the power consumed by the pump increase rapidly with the increase in R123 mass flow rate. A small part of the tested data is used to identify the empirical parameters in the tank model, the pump model and especially the expander model. The others are adopted to validate the models.

4.2. Verification of the mathematical model

The inlet temperature and pressure of the tank at one tested point is used to identify the amount of non-condensable gas in the tank. $n_{gas} = 2.17$mol is obtained. Then, Eq. (5) is applied to predict the tank pressure under other conditions. Fig. 6(a) shows the validation of the tank model. The maximum deviation between the tested pressures and the predictions by the model is 5.5%.

The cooling tower model is quite important in the present work to take account of the environment effect on the performance of the cycle. The validation of the cooling tower model is given in Fig. 6(b). All the points are calculated at a constant air humidity of 50%, which is the average value during the day we perform the test. The outlet temperatures of the cooling tower (temperature of cooling water at the condenser inlet) at most points are predicted with a maximum absolute error of 1 K. A few points have the error of 2 K. Compared to the air temperature variation of tens of degrees, this model is accurate enough.

The evaporator in the prototype is a double-pipe heat exchanger. Temperatures of conductive oil and R123 along the pipe are tested. Fig. 6(c) shows that the predictions by the model agree well with the tested temperature profile. The typical three heat transfer zones: the liquid zone, the two-phase zone and the vapor zone are well predicted. Due to the gradual change of the oil properties and the heat flux at different location along the pipe, the temperature profile is not linear.

Perform the simulation under the same conditions of the test, the comparison of the modeled and the tested shaft power is given in Fig. 6(d). During the simulation, errors transfer between different sub-models, accumulate or offset in the cycle. As a result, the maximum deviation is about 10%. Additionally, we also provide a comparison of the tested and modeled results in Table 5 for temperatures and pressures at different locations of the loop as well as the shaft power of the expander. The comparisons prove that the model is accurate enough for extended simulations of the prototype under other operation conditions. In the followed sections, this model is used to analyze the sensitivity of the operation parameters and the potential of optimization measures.

4.3. Effect of operation conditions on cycle performance

Four parameters are defined to represent the operation conditions: the temperature and mass flow rate of the conductive oil, the temperature and humidity of the environment (typically air). Although the tested data show that the liquid entrainment reduces the shaft power at low superheat degrees, for a model work, several works [4,31] have proved that the saturated vapor at the expander inlet would give the best performance. Thus, the fluid is also controlled at the saturated state in the present simulation in order to facilitate the comparison of cycle performance under different operation parameters. In this case, the mass flow rate of the working fluid is the only controlled variable.

4.3.1. Temperature and mass flow rate of the conductive oil

Fig. 7 shows the effect of the conductive oil temperature on cycle performance. In Fig. 7(a), it is seen that the increase in the mass flow rate leads to the increase in the expander rotating

Table 5
Comparison of tested and modeled results.

Parameters	Value								
m (kg/h)	Control	656	653	653	650	650	650	648	648
N_t (rpm)	Control	2569	2156	1782	1498	1215	1075	940	831
$T_{exp,in}$ (°C)	tested	142.93	141.14	137.79	132.47	124.65	121.6	120.3	121.29
	modeled	143.54	141.75	136.46	131.90	124.62	120.40	119.63	124.08
$P_{exp,in}$ (kPa)	tested	781.92	848.33	928.53	1008.27	1091.58	1133.33	1168.26	1212.58
	modeled	750.00	820.00	910.00	1000.00	1100.00	1150.00	1180.00	1290.00
$T_{exp,out}$ (°C)	tested	119.5	112.5	105.3	96.43	86.17	81	74.6	66.7
	modeled	118.68	112.60	103.45	95.78	85.04	78.86	69.98	72.98
$P_{exp,out}$ (kPa)	tested	251.29	248.33	246.33	243.22	238.7	236.97	233.95	232.01
	modeled	254.66	251.17	247.59	243.60	240.09	237.76	234.15	234.45
$T_{con,out}$ (°C)	tested	18.15	18.25	18.23	17.84	17.91	18.01	17.3	17.27
	modeled	19.74	19.55	19.29	19.06	18.98	18.86	18.61	18.55
$P_{con,out}$ (kPa)	tested	144.01	143.61	142.16	140.51	139.53	139.44	137.93	137.84
	modeled	149.90	147.53	145.14	142.47	140.66	139.40	137.91	137.21
$T_{evp,in}$ (°C)	tested	19.43	20.13	20.09	19.9	19.74	19.91	19.48	19.07
	modeled	20.74	20.55	20.29	20.06	19.98	19.86	19.61	19.55
$P_{evp,in}$ (kPa)	tested	799.64	866.54	940.77	1019.29	1100.63	1140.80	1180.36	1219.52
	modeled	770.00	840.00	930.00	1020.00	1120.00	1170.00	1200.00	1320.00
W_{exp} (W)	tested	1395	2036	2414	2650	2651	2553	2399	2297
	modeled	1474.05	1975.97	2325.36	2505.24	2572.49	2552.13	2407.45	2465.35

speed for a specified oil temperature. This is because a higher rotating speed is required to balance the larger R123 vol flow rate. Fig. 7(b) shows that the expander shaft power also becomes higher due to the increase in the expander rotating speed, and reaches the maximum value at an optimum mass flow rate. Then, it decreases with the further growth in expander rotating speed because the higher R123 mass flow rate makes the vapor at the expander inlet saturated at a much lower shaft torque. As the oil temperature goes up, the heat transfer in the evaporator is enhanced. For a specified expander rotating speed, the outlet vapor reaches the saturated state at a larger mass flow rate. Consequently, the pressure and temperature at the expander inlet both become higher. The performance of the expander is improved. The maximum shaft power increases from 1453 W at oil temperature of 130 °C to 3926 W at 170 °C, nearly 2.7 times higher. Due to the increase in the evaporator heat flux and power consumed by the fluid pump, the thermal efficiency exhibits a gradual increase with the oil temperature, as shown in Fig. 7(c).

Fig. 8 shows the effect of the mass flow rate of conductive oil on the cycle performance. It is found that the effect of increasing the oil mass flow rate is similar to that of increasing the oil temperature. The higher oil mass flow rate reduces the temperature drop of oil from the inlet to the outlet. Thus, the higher fluid pressure and temperature at the expander inlet can be obtained. When the oil mass flow rate is below 3000 kg/h, the increase in the oil mass flow rate can significantly improve the cycle performance. Comparatively, the performance of the cycle is less sensitive to the variation of the oil mass flow rate when it is increased from 3000 kg/h to 5000 kg/h. This indicates the variation of the oil temperature drop becomes gentle with the further increase in the oil mass flow rate. Generally speaking, a larger oil mass flow rate leads to a better cycle performance. The maximum shaft power increases from 2017W at 1500 kg/h to 3870 W at 5000 kg/h, nearly 1.9 times higher. The maximum system thermal efficiency gradually increases from 4.56% to 5.25%.

4.3.2. Temperature and humidity of the air

In this section, the air humidity is kept at 50% when simulating the effect of air temperature. In turn, the air temperature of 5 °Cis maintained when model the effect of air humidity. The values of 50% and 5 °C are the measured environment conditions during the test. Fig. 9 shows the effect of air temperature on the system performance. The heat transfer in the condenser is weakened by the increasing air temperature. Thus, the backpressure of the expander becomes higher. It can be seen in Fig. 9(a) that the external pressure ratio is reduced with the increase in air temperature for a specified R123 mass flow rate. Reflected in Fig. 9(b), the shaft power exhibits a gradual decrease from 2630 W to 2459 W with air temperature increasing from −5 °C to 35 °C. The air temperature has quite limited effect on the system thermal efficiency because the heat flux in the evaporator also decreases with the rising air temperature. Fig. 10 shows the effect of air humidity on the system performance. It is found that the effect of humidity is even weaker than that of the air temperature. This is because two mechanisms contribute to the heat release in the closed cooling tower. One is the single-phase convective heat transfer between the deluge water film and the air; the other is the evaporation of the deluge water. When the air temperature is low, the heat release is primarily attributed to the single-phase convective heat transfer. Consequently, the variation of the air humidity has limited effect on the operation and performance of the cycle.

It is noted that the insensitivity of the cycle performance to the air temperature and humidity indicates the mismatch among the components in the prototype: the too small built-in volume ratio of the expander and the high expander backpressure. The small built-in volume ratio makes the expander mainly work at the under-expansion state, reducing its capacity for doing work. The high expander backpressure is due to the non-condensable gas in the tank and the resistance of vapor flowing through the regenerator, especially the latter, attributing most of the expander backpressure. It results in the insensitivity of the cycle performance to the air temperature and humidity as these two factors mainly affect the pressure in the tank.

4.4. Effect of optimization measures on cycle performance

The results and analysis in section 4.1 and 4.3 indicate that the design of the present prototype can be improved by optimizing the weak links in the loop, mainly on three aspects: (1) Reducing the backpressure of the expander; (2) Increasing the built-in volume ratio of the expander; (3) Increasing the heat transfer area of the evaporator. Effects of the above optimization measures are evaluated by the present model in sequence. It means that the simulation of “Increasing the built-in volume ratio of the expander” is

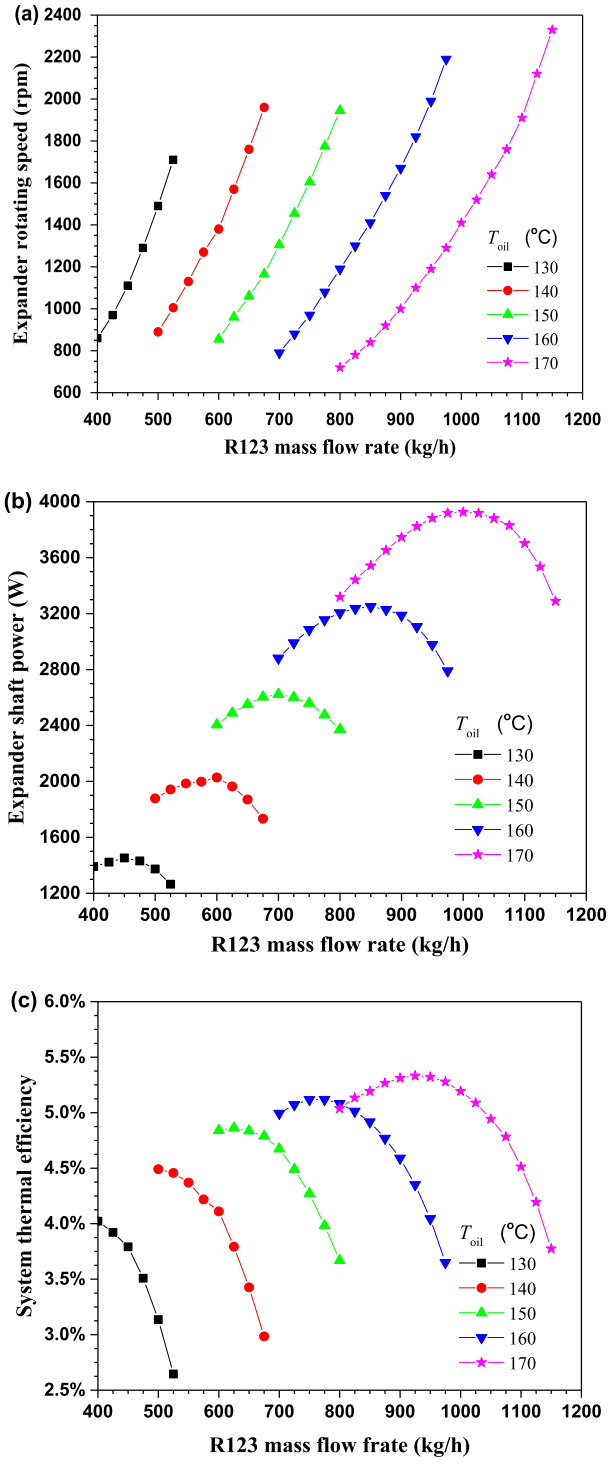

Fig. 7. Effect of the conductive oil temperature on system performance.

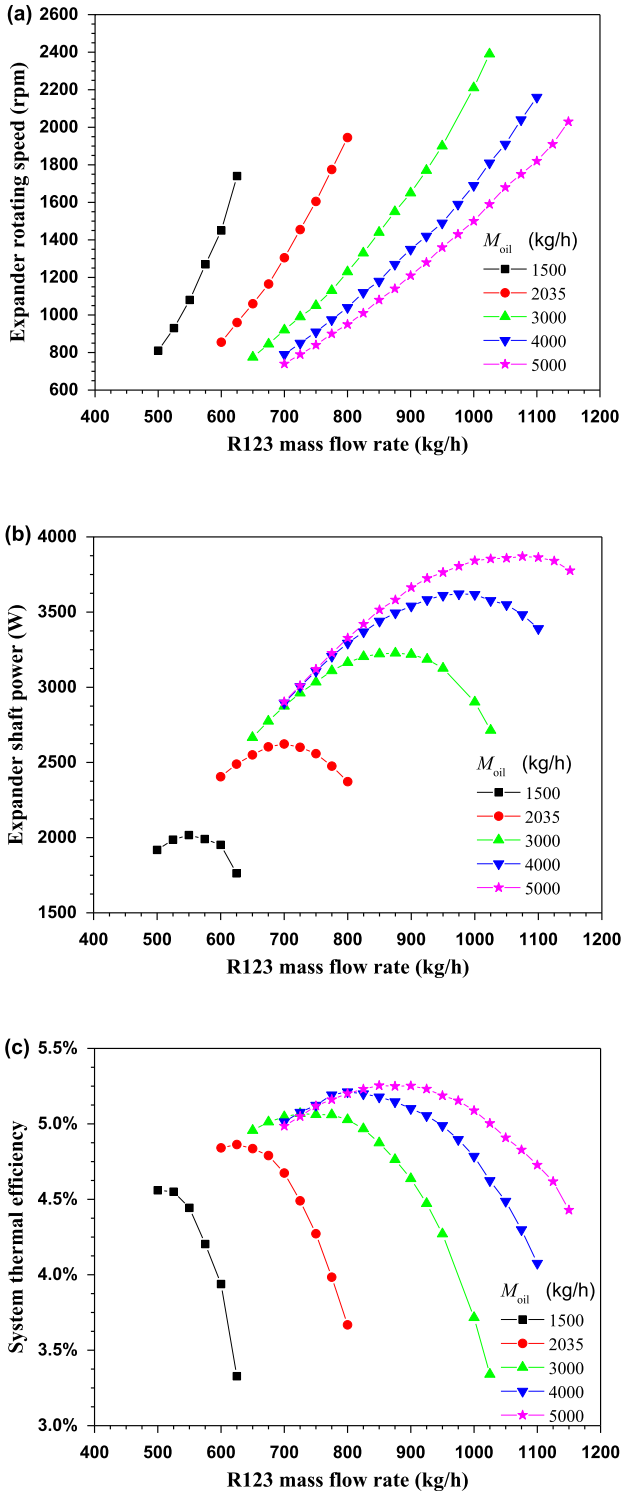

Fig. 8. Effect of the conductive oil mass flow rate on system performance.

performed based on the results of "Reducing the backpressure of the expander". And the simulation of "Increasing the heat transfer area of the evaporator" gives the optimum cycle design.

4.4.1. Reducing the backpressure of the expander

The effect of expander backpressure on system performance is evaluated and shown in Fig. 11. In the present prototype, the non-condensable gas in the tank and the flow of R123 vapor through the regenerator are closely related to the backpressure of the expander. It is seen that decreasing the amount of non-condensable gas in the tank can improve the system performance. The shaft power and thermal efficiency both become higher. If a bypass for the vapor phase is installed on the regenerator, represented by the blue line in Fig. 11, the shaft power and thermal efficiency could be further optimized. For the variation of R123 mass flow rate in the test, the pressure drop in the regenerator is about 70 kPa–130 kPa. By decreasing the backpressure of

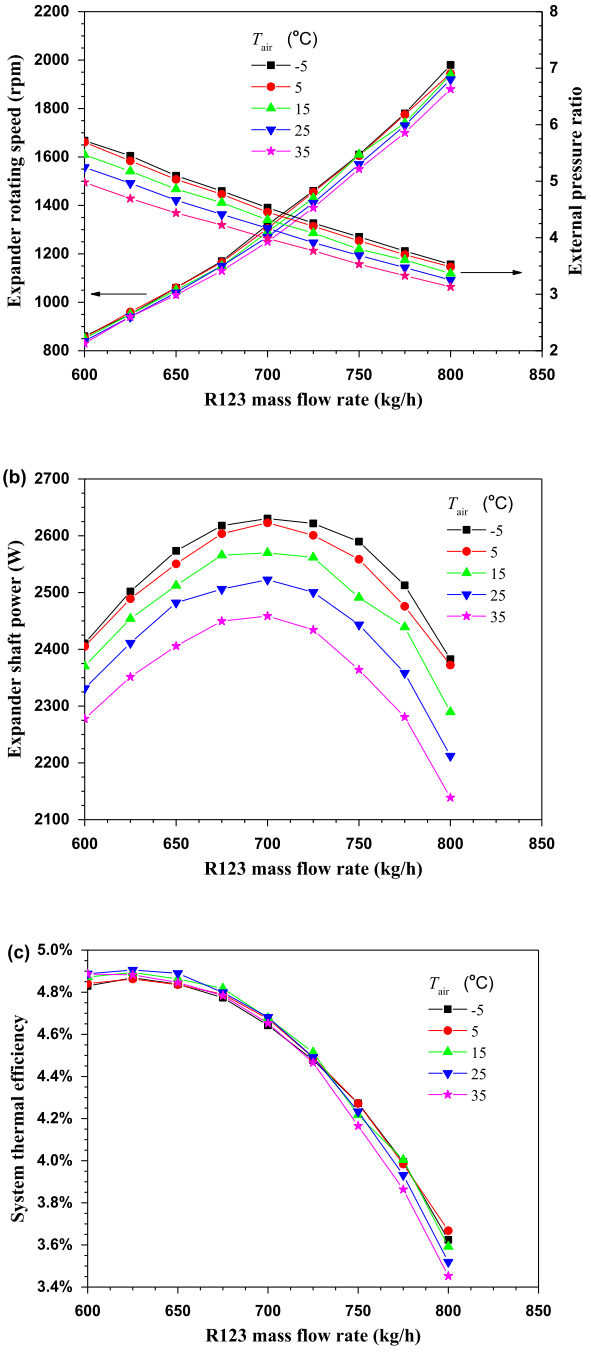

Fig. 9. Effect of the air temperature on system performance.

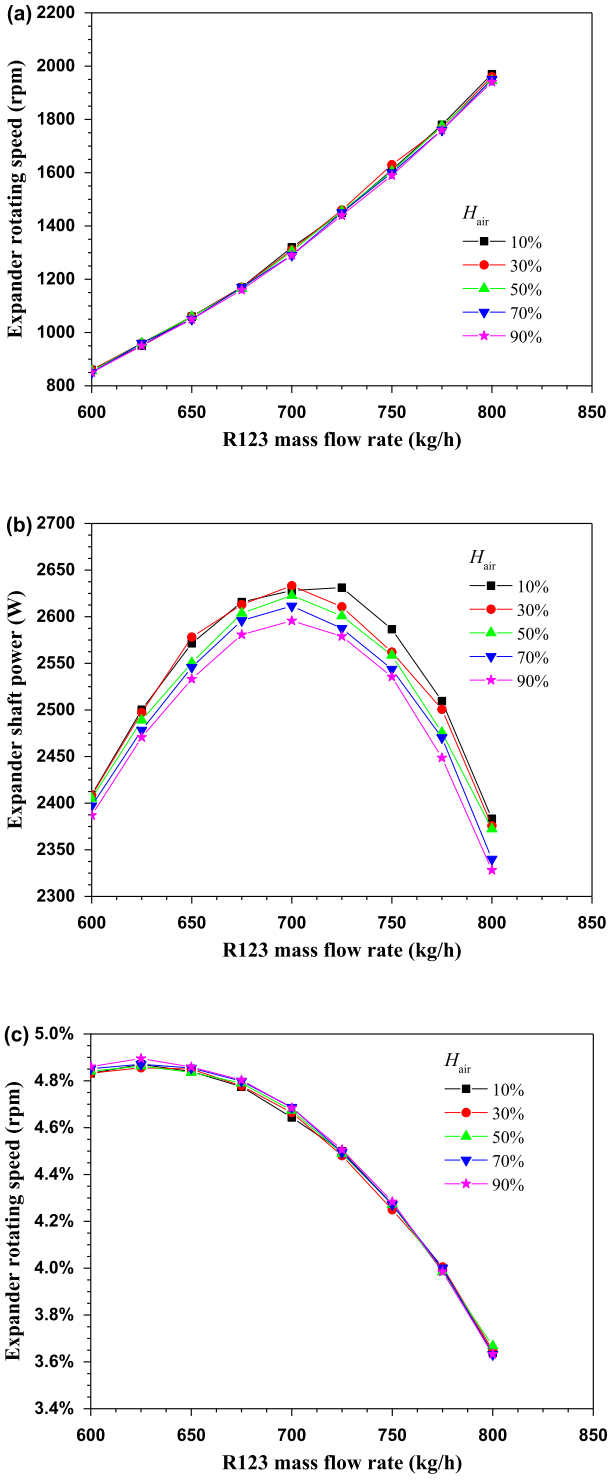

Fig. 10. Effect of the air humidity on system performance.

the expander, the maximum shaft power increase from 2623 W to 3626 W, about 38% higher. The maximum system thermal efficiency increases from 4.86% to 6.74%. Besides, Fig. 11(a) shows that reducing the backpressure of the expander has quite limited effect on the rotating speed. This will benefit the control of the cycle.

4.4.2. Increasing the built-in volume ratio of the expander

Fig. 12 shows the effect of the optimization measure 2: increasing the built-in volume ratio on the cycle operation and performance. It can be seen in Fig. 12(a) that the external pressure ratio varies from 6 to 13. The built-in volume ratio of the expander in test is 2.27. It indicates that the expander works at the under-expansion state. The too small built-in volume ratio weakens the expander's capacity to do work. Thus, choosing an expander with a larger built-in volume ratio can improve the system performance. For the scroll expander, the built-in volume ratio is generally below 7. In the present model, the effect of varying built-in volume ratio from 2.27 to 6 is evaluated while other parameters of the expander remain unchanged. Fig. 12(b) shows that the shaft power can be further improved by a larger built-in volume ratio, compared with Fig. 11(b). The maximum shaft power of 5078 W is

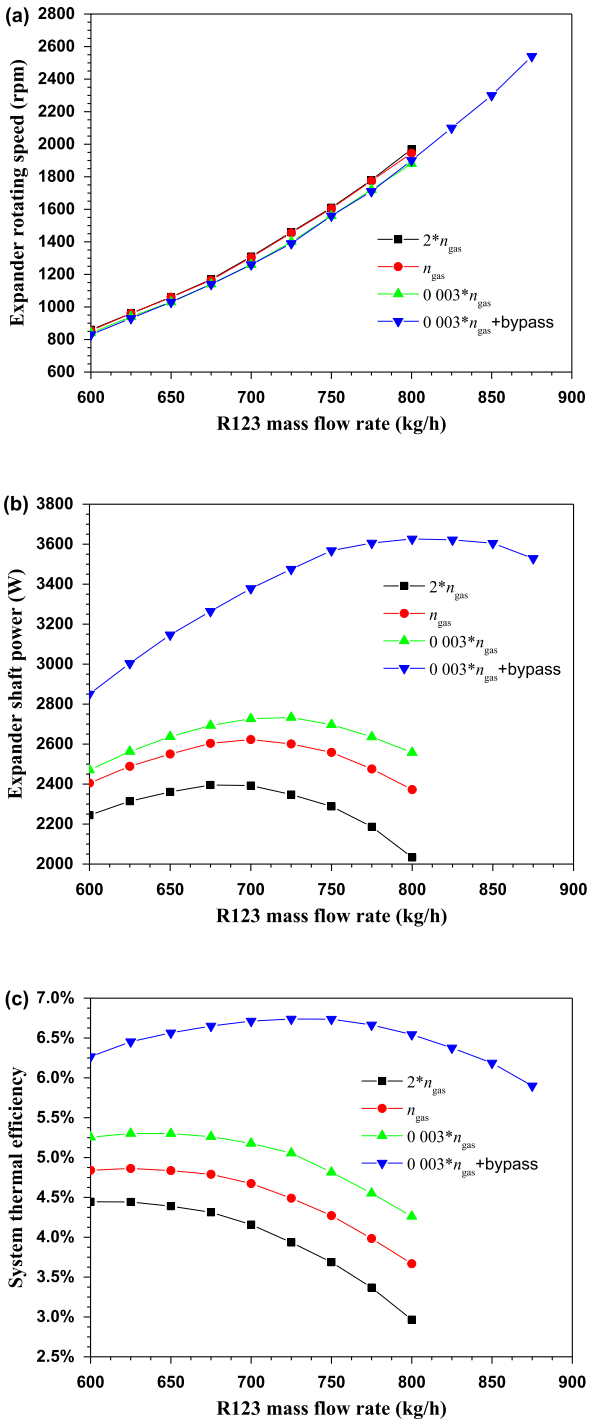

Fig. 11. Effect of the optimization measure 1: back pressure, on system performance.

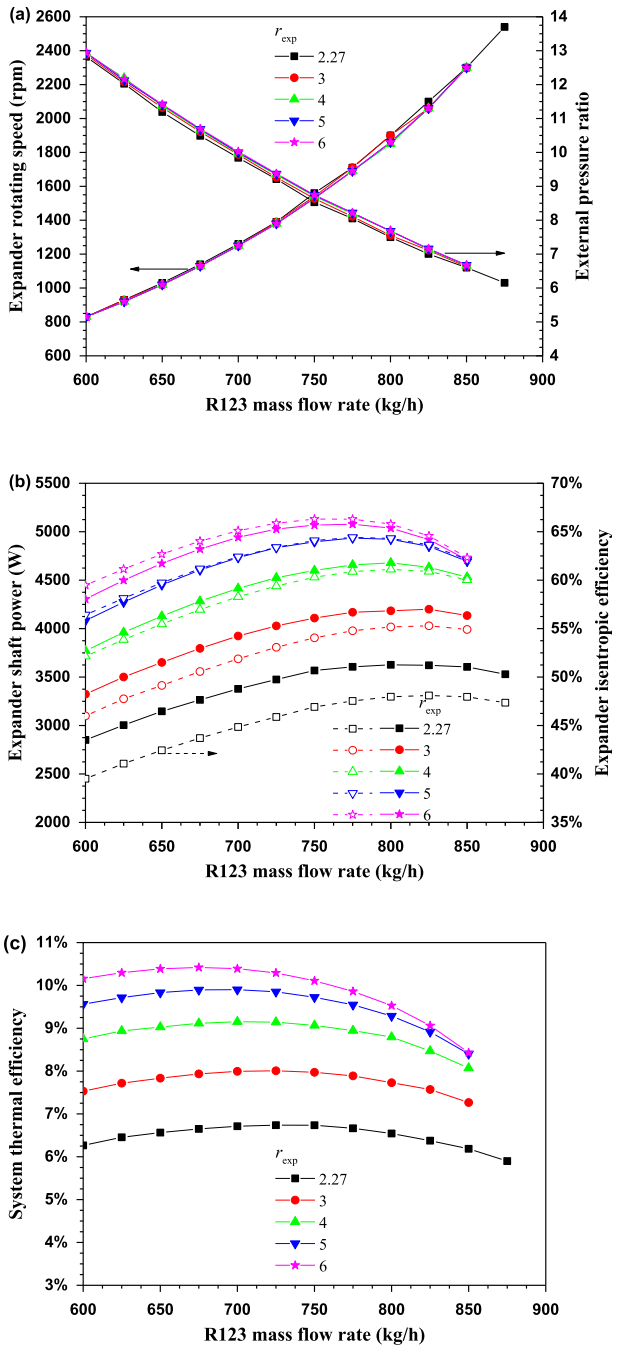

Fig. 12. Effect of the optimization measure 2: built-in volume ratio on system performance.

obtained at the built-in volume ratio of 6. The isentropic efficiency of the expander is calculated by Eq. (24) and plotted in Fig. 12(b). It is seen that the expander's capacity of doing work is improved with the increase in the expander built-in volume ratio. The largest achieved isentropic efficiency of the expander is 66% at the built-in volume ratio of 6, compared to 48% at the built-in volume ratio of 2.27. The system thermal efficiency also increases with the increasing built-in volume ratio as the heat flux in evaporator is not sensitive with the variation of the built-in volume ratio. The maximum thermal efficiency is about 10.42%. Similar to trends in Fig. 11(a), the variation of the built-in volume ratio has quite limited effect on the trend of rotating speed vs. R123 mass flow rate shown in Fig. 12(a).

4.4.3. *Increasing the heat transfer area of the evaporator*

Based on the analysis of tested data in section 4.1 and modeled results in section 4.3, the evaporator area should be increased to operate the ORC system at a larger flow rate than the designed

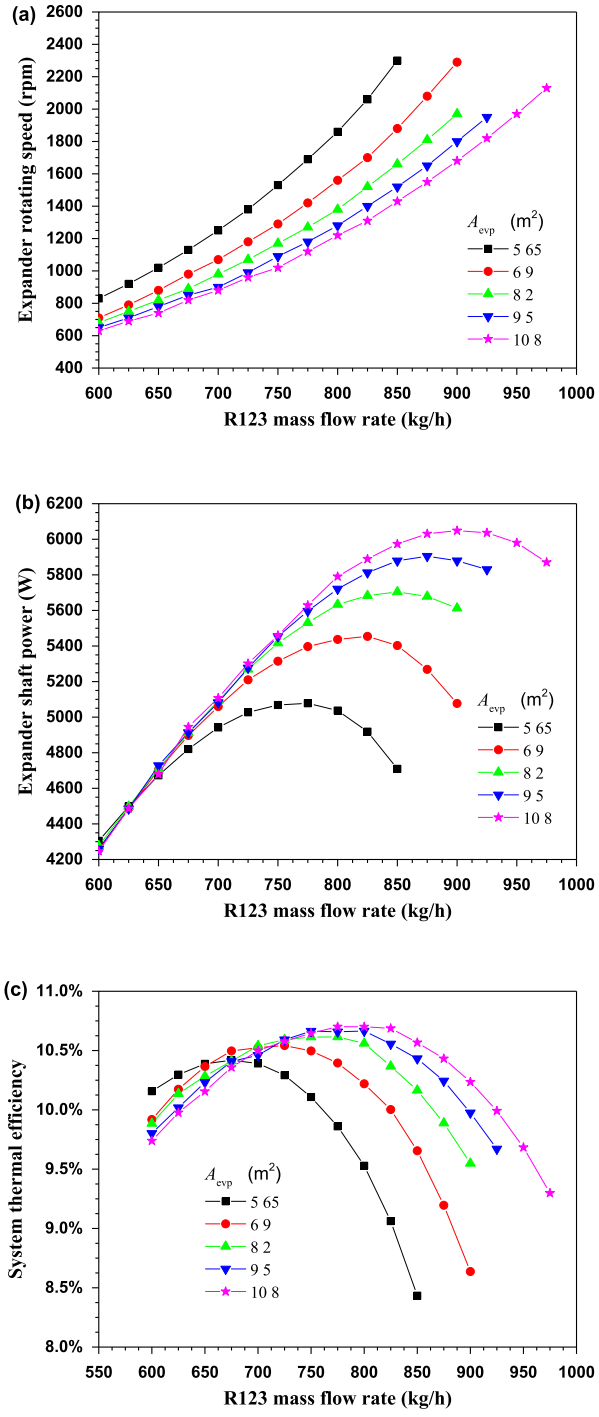

Fig. 13. Effect of the optimization measure 3: evaporator heat transfer area on system performance.

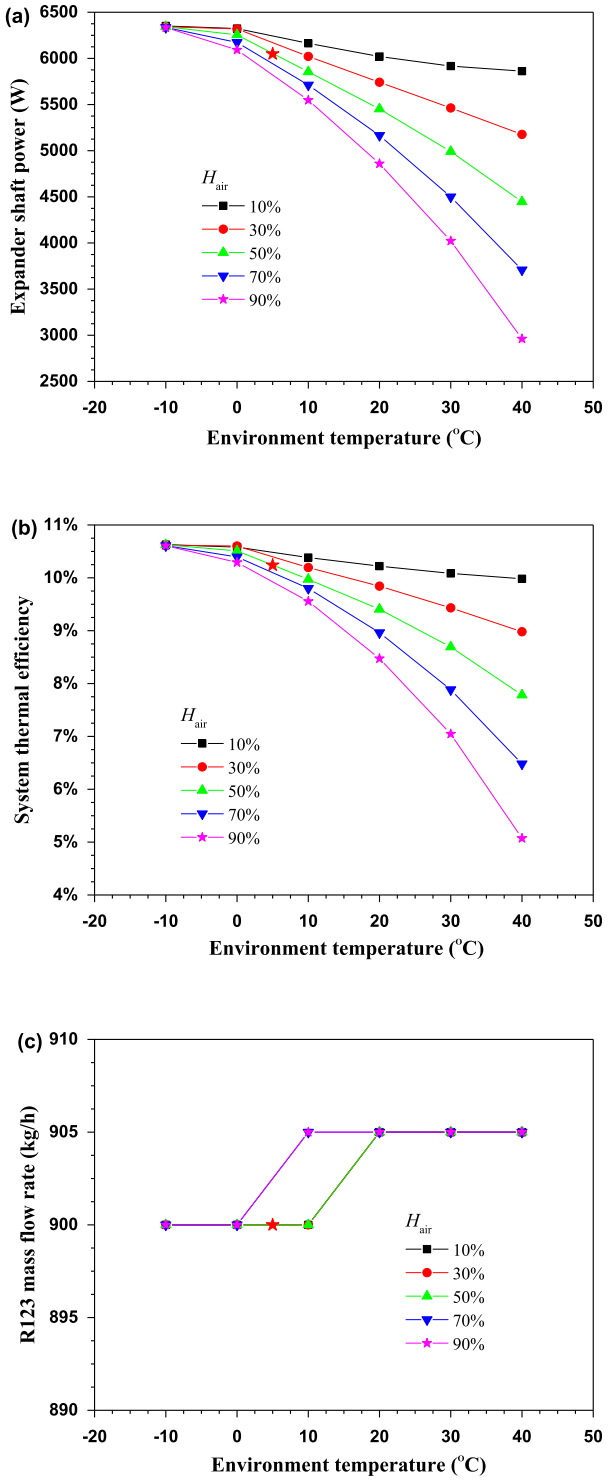

Fig. 14. Influence of the air temperature and humidity on system performance and operation of the optimum design (the red star point). (For interpretation of the references to colour in this figure legend, the reader is referred to the web version of this article.)

value. Increasing the area of evaporator can supply enough vapor with higher temperature and pressure to the expander. Reflected in Fig. 13(a), the expander rotating speed becomes lower with the increase in the evaporator area for a specified R123 mass flow rate. It indicates that the larger shaft torque can be obtained, and the performance of the expander can be improved.

It is noted that the increase in the evaporator area also means the increase in the investment. Considering both the performance and the economics of the ORC system, we set the criterion as that the pinch temperature of heat transfer process in the evaporator should be higher than 5 °C. Accordingly, the maximum area is evaluated to be 10.8 m^2 in the present model. Fig. 13(b) shows that the final optimized shaft power is 6049 W, about 2.3 times higher than the initial value of 2623 W. The corresponding system thermal efficiency is 10.24%, about 2.2 times higher than the initial value of 4.67%. Due to the increase in the heat flux, the system thermal

efficiency only exhibits a gradual increase with R123 mass flow rate, shown in Fig. 13(b). The maximum thermal efficiency is 10.70%.

4.5. Effect of the environment on the optimum cycle design

Based on the three optimization measures above, the optimum cycle design is achieved with the performance: expander shaft power of 6049 W and corresponding system thermal efficiency of 10.24%. The two control variables at the optimum point are set as 900 kg/h and 1680 rpm. In this section, the effect of environment conditions, represented by the air temperature and humidity, on the operation and performance of the optimum system design is discussed. This is closely related to the long-time operation characteristics of the ORC system. Corresponding to the weather in Beijing, the variation of the air temperature and humidity in the present model is set from −10 °C to 40 °C and from 10% to 90%, respectively. As the constant rotating speed mode is the common adopted control mode for the ORC system. In the present simulation, the expander rotating speed is kept at 1680 rpm. The fluid state at the expander inlet is kept saturated by adjusting the R123 mass flow rate. And the minimum step is 5 kg/h, corresponding about 0.1 Hz on the frequency converter. The overheating degree below 0.5 °C or the mass fraction of liquid phase less than 0.5% is allowed.

Fig. 14 shows the effect of air temperature and humidity on the expander shaft power, system thermal efficiency and R123 mass flow rate. The red star represents the optimum cycle design achieved in section 4.4. It can be seen in Fig. 14(a) and (b) that the shaft power and thermal efficiency decrease significantly with the increase in air temperature and humidity. At the air humidity of 50%, the expander shaft power is reduced from 6343.4 W to 4446.3 W by the increasing air temperature from −10 °C to 40 °C. This result agrees well with the tested data in Dong's work [35] for the ORC operating in winter and summer.

It is very interesting that all the curves representing shaft power or thermal efficiency converge at one point at the air temperature of −10 °C. This means the effect of air humidity on the cycle performance could be neglected when the air temperature is below −10 °C. Conversely, the air humidity becomes more effective with the increase in the air temperature. At the air temperature of 40 °C, the shaft power decreases from 4446.3 W to 2961.5 W with the air humidity rising from 50% to 90%. The system thermal efficiency is reduced from 7.79% to 5.07%. Thus, the performance of the ORC system will be significantly reduced with the season shift from winter to summer.

Fig. 14(c) shows that the environment parameters have quite limited effect on the R123 mass flow rate. The mass flow rate is 900 kg/h for the air temperature below zero, and is adjusted to 905 kg/h only when the air temperature is higher than 10 °C or the air humidity higher than 70%. Results in Fig. 14(c) indicate that the operation of the present optimized ORC system under the constant rotating speed mode is quite simple. If the cycle and expander have a little greater tolerance for the overheating and liquid entrainment at the expander inlet, the control scheme could have only one variable: the expander rotating speed.

5. Conclusions

This paper presents the experimental and modeling investigation of an Organic Rankine Cycle (ORC) based on a scroll expander. The main findings are summarized as follows:

(1) The tested prototype can offer a maximum shaft power of 2.65 kW. And the corresponding system thermal efficiency is 5.64%. The small built-in volume ratio and higher back pressure of the expander results in the insensitivity of the prototype performance to the variation of environment temperature and humidity.
(2) The system performance can be significantly improved by optimizing the match among different components. The maximum model predicted shaft power obtained from the optimum cycle design is 6.05 kW, more than double the prototype level. The corresponding thermal efficiency is 10.7%, about 1.9 times higher than the prototype level.
(3) Performance of the optimum cycle design is quite sensitive to the environment conditions. The effect of air humidity can be neglected at the air temperatures below −10 °C. Conversely, the expander shaft power decreases by more than one third from winter to summer. It is suggested to evaluate the cycle performance at extreme environment conditions when designing an ORC system.

Acknowledgements

This work was supported by the National Natural Science Foundation of China (No. 51306048 and No. 51210011).

References

[1] Hung TC, Shai TY, Wang SK. A review of organic Rankine cycles (ORCs) for the recovery of low grade waste heat. Energy 1997;22(7):661–7.
[2] Hung T-C. Waste heat recovery of organic Rankine cycle using dry fluids. Energy Convers Manag 2001;42:539–53.
[3] Clemente S, Micheli D, Reini M, Taccani R. Energy efficiency analysis of Organic Rankine Cycles with scroll expanders for cogenerative applications. Appl Energy 2012;97:792–801.
[4] Yamamoto T, Furuhata T, Arai N, Mori K. Design and testing of the organic Rankine cycle. Energy 2001;26:239–51.
[5] Li MQ, Wang JF, He WF, Gao L, Wang B, Ma SL, et al. Construction and preliminary test of a low-temperature regenerative Organic Rankine Cycle (ORC) using R123. Renew Energy 2013;57:216–22.
[6] Pei G, Li J, Li Y, Wang D, Ji J. Construction and dynamic test of a small-scale organic rankine cycle. Energy 2011;36:3215–23.
[7] Li J, Pei G, Li Y, Wang D, Ji J. Energetic and exergetic investigation of an organic Rankine cycle at different heat source temperatures. Energy 2012;38:85–95.
[8] Li J, Pei G, Li Y, Wang D, Ji J. Examination of the expander leaving loss in variable organic Rankine cycle operation. Energy Convers Manag 2013;65:66–74.
[9] Bracco R, Clemente S, Micheli D, Reini M. Experimental tests and modelization of a domestic-scale ORC (organic Rankine cycle). Energy 2013;58:107–16.
[10] Minea V. Power generation with ORC machines using low-grade waste heat or renewable energy. Appl Therm Eng 2014;69(1–2):143–54.
[11] Wang XD, Zhao L, Wang JL. Experimental investigation on the low-temperature solar Rankine cycle system using R245fa. Energy Convers Manag 2011;52:946–52.
[12] Wang JL, Zhao L, Wang XD. An experimental study on the recuperative low temperature solar Rankine cycle using R245fa. Appl Energy 2012;94:34–40.
[13] Zheng N, Zhao L, Wang XD, Tan YT. Experimental verification of a rolling-piston expander that applied for low-temperature Organic Rankine Cycle. Appl Energy 2013;112:1265–74.
[14] Li L, Ge YT, Luo X, Tassou SA. Experimental investigations into power generation with low grade waste heat and R245fa Organic Rankine Cycles (ORCs). Appl Therm Eng 2017;115:815–24.
[15] Uusitalo A, Honkatukia J, Turunen-Saaresti T. Evaluation of a small-scale waste heat recovery organic Rankine cycle. Appl Energy 2017;192:146–58.
[16] Miao Z, Yang X, Xu J, Zou J. Development and dynamic characteristics of an organic Rankine cycle. Chin Sci Bull 2014;59:1–12.
[17] Miao Z, Xu J, Yang X, Zou J. Operation and performance of a low temperature organic Rankine cycle. Appl Therm Eng 2015;75:1065–75.
[18] Yang X, Xu J, Miao Z, Zou J, Yu C. Operation of an organic Rankine cycle dependent on pumping flow rates and expander torques. Energy 2015;90:864–78.
[19] Andersen WC, Bruno TJ. Rapid screening of fluids for chemical stability in organic Rankine cycle applications. Ind. Eng Chem Res 2005;44:5560–6.

[20] He C, Liu C, Gao H, Xie H, Li YR, Wu SY, et al. The optimal evaporation temperature and working fluids for subcritical organic Rankine cycle. Energy 2012;38:136–43.
[21] Li YR, Wang JN, Du MT. Influence of coupled pinch point temperature difference and evaporation temperature on performance of organic Rankine cycle. Energy 2012;42:503–9.
[22] Liu BT, Chien KH, Wang CC. Effect of working fluids on organic Rankine cycle for waste heat recovery. Energy 2004;29:1207–17.
[23] Liu C, He C, Gao H, Xie H, Li YR, Wu SY, et al. The environmental impact of organic Rankine cycle for waste heat recovery through life-cycle assessment. Energy 2013;56:144–54.
[24] Mago PJ, Chamra LM, Somayaji C. Performance analysis of different working fluids for use in organic Rankine cycles. Proc Inst. Mech Eng Part A J Power Energy 2007;221:255–64.
[25] Saleh B, Koglbauer G, Wendland M, Fischer J. Working fluids for low-temperature organic Rankine cycles. Energy 2007;32:1210–21.
[26] Tchanche BF, Papadakis G, Lambrinos G, Frangoudakis A. Fluid selection for a low-temperature solar organic Rankine cycle. Appl Therm Eng 2009;29:2468–76.
[27] Xu J, Liu C. Effect of the critical temperature of organic fluids on supercritical pressure Organic Rankine Cycles. Energy 2013;63:109–22.
[28] Pezzuolo A, Benato A, Stoppato A, Mirandola A, The ORC-PD. Aversatile tool for fluid selection and Organic Rankine Cycle unit design. Energy 2016;102:605–20.
[29] Wei D, Lu X, Lu Z, Gu J. Dynamic modeling and simulation of an Organic Rankine Cycle (ORC) system for waste heat recovery. Appl Therm Eng 2008;28:1216–24.
[30] Lemort V, Quoilin S, Cuevas C, Lebrun J. Testing and modeling a scroll expander integrated into an Organic Rankine Cycle. Appl Therm Eng 2009;29:3094–102.
[31] Quoilin S, Lemort V, Lebrun J. Experimental study and modeling of an Organic Rankine Cycle using scroll expander. Appl Energy 2010;87:1260–8.
[32] Declaye S, Quoilin S, Guillaume L, Lemort V. Experimental study on an open-drive scroll expander integrated into an ORC (Organic Rankine Cycle) system with R245fa as working fluid. Energy 2013;55:173–83.
[33] Benato A, Kaern MR, Pierobon L, Stoppato A, Haglind F. Analysis of hot spots in boilers of organic Rankine cycel units during transient operation. Appl Energy 2015;151:119–31.
[34] Proctor MJ, Yu W, Kirkpatrick RD, Young BR. Dynamic modelling and validation of a commercial scale geothermal organic rankine cycel power plant. Geothermics 2016;61:63–74.
[35] Dong SM, Zhang YF, He ZL, Yu XH, Zhang Y, Kong XR. Optimum design method of Organic Rankine Cycle system based on semi-empirical model and experimental validation. Energy Convers Manag 2016;108:85–95.
[36] Ziviani D, Gusev S, Lecompte S, Groll EA, Braun JE, Horton WT, et al. Optimizing the performance of small-scale organic Rankine cycel that utilizes a single-screw expander. Appl Energy 2017;189:416–32.
[37] Korolija I, Greenough R. Modelling of the influence of climate on the performance of the organic Rankine cycle for industrial waste heat recovery. Energies 2016;9(335):1–20.
[38] Hasan A, Siren K. Performance investigation of plain circular and oval tube evaporatively cooled heat exchangers. Appl Therm Eng 2004;24(5–6):777–90.
[39] PR O, TR E. The heat and mass transfer characteristics of evaporative coolers. Chem Eng Prog Symp 1961;57(32):138–49.
[40] T M RI, H M. Experimental study of an evaporative cooler. Int Chem Eng 1967;7(4):727–32.
[41] G V. New equations for heat mass transfer in turbulent pipe and channel flows. Int Chem Eng 1976;16:359–68.
[42] GK E, WRH S. A general correlation for fow boiling in tubes and annuli. Int J Heat Mass Transf 1986;29(3):351–8.
[43] GK E, WRH S. Simplified general correlation for saturated flow boiling and comparisons of correlations with data. Chem Eng Res Des 1987;65:148–56.
[44] SM. M. Chart correlation for saturated boiling heat transfer : equations and further study. ASHRAE Trans 1982;88(Part 1):185–96.
[45] Y YY, LH C, L. TF. Condensation heat transfer and pressure drop of refrigerant R-134a in a plate heat exchanger. Int J Heat Mass Transf 1999;42:993–1006.
[46] DS K, S B, R W. Dynamic behavior of plate heat exchangers - experiments and modeling. J Heat Transf 1995;117(4):859–64.
[47] A WW, D HA, C O. Condensation heat transfer within horizontal tubes. Chem Eng Prog 1958;54(10):89–90.

Nomenclature

List of symbols

A: area, m^2
Bo: boiling number
d: hydraulic diameter, m
h: heat transfer coefficient, $W/(m^2K)$
h_d: mass transfer coefficient, kg/m^2
H: specific enthalpy, J/kg
i: enthalpy of vaporization, J/kg
k: thermal conductivity, W/(mK)
m: mass flow rate, kg/h
M: molecular weight, g/mol
N: rotating speed, rpm
Nu: Nusselt number exp expander
p_r: ratio of the saturation pressure to the critical pressure
P: pressure, Pa
Pr: Prandtl number
Q: heat transfer rate, W
r: ratio
Re: Reynolds number
s: specific entropy, J/(kgK)
T: shaft torque, $N \cdot m$
T: temperature, °C
v: specific volume, m^3/kg
V: volume, m^3
W: power, W

Greek letters

η: efficiency
λ: thermal conductivity
ρ: density, kg/m^3
ω: Moisture content
ξ: coefficient considering the effect of m on Ah_{in}, J/(kg K)

Subscripts

ad: adiabatic
air: air
amb: ambient
cw: cooling water
d: design
dw: deluge water
eva: evaporator
ex: exit
gas: non-condensable gas
h: high temperature
in: inlet, inside
l: low temperature
L: liquid phase
me: measured
nb: nucleate boiling
Out: outlet
p: pressure
s: isentropic process
sat: saturated state
su: suction
t: turbine, expander
tp: two phase
w: water, wall